Atomisation of an acoustically levitated droplet: Experimental observations of a myriad complex phenomenon: supplementary Information (SI)

SUNIL KUMAR SAROJ, ROCHISH M. THAOKAR

1. INTRODUCTION

The SI attempts to further explain and supplement several aspects of our observations discussed in the main manuscript. The corresponding videos are provided in the captions of the respective figures.

2. ADDITIONAL DETAILS ABOUT THE METHODOLOGY AND EXPERIMENTS

The side and top imaging was conducted at the field view of 1.46 mm $\times$ 0.73 mm and 1.64 mm $\times$ 0.82 mm, respectively at 140,000 fps to capture the instability on the liquid interface as well as to measure the diameter of the droplet produced during atomisation. The corresponding spatial resolutions are 5.7 μm/pixel and 6.4 μm/pixel, respectively. The images captured at 14485 fps, 48000 fps and 72000 fps has a field view of 5.55 mm $\times$ 4 mm, 3.5 mm $\times$ 1.75 mm and 2 mm $\times$ 1.5 mm, respectively. A scale bar has been inserted for each field of view to convert the pixel into mm.

3. FURTHER DISCUSSION ON RESULTS

Figure S1 shows the top and side view images of the sequence of events starting from levitation, stretching thinning at the edges followed by the equatorial atomisation of the acoustically levitated droplet. The droplet flattening occurs when an injected droplet is levitated at the node of a standing wave. The droplet first transforms from a spherical shape to a flattened disc shape (see S1 (a) and (b)) and is termed the stretching regime. This is followed by the thinning regime that refers to the thinning of the edge region (equatorial region of the droplet) ((see S1 (c)). Atomization at the edge refers to the disintegration of the liquid sheet at the edge (see S1 (d)) Secondary breakup of the convexly deflect stretched droplet sheet occurs at the end of edge atomisation during the deceleration of the atomized sheet. The bag breakup occurs in 4 different ways: umbrella breakup, bag breakup, bubble breakup, and multistage breakup which is discussed in the main manuscript. In the following sub-sections, we discuss the various aspects of levitation and breakup phenomena.

A. Droplet Levitation in acoustic trap and critical We

Figure S2 shows the experimental data for the steady deformation of a stable levitated droplet (without breakup) placed in an acoustic standing wave. The droplet assumes an oblate spheroidal shape and the corresponding variation of its deformation is represented by $(\frac{2R}{d_0})$ at different We. Here $2R$ is the length of the principal-major axis of the oblate spheroidal droplet (R termed as radius of the oblate droplet in this work). The

value of $2R$ and thereby the deformation of the droplet increases with increasing We along with a corresponding reduction of the length of the principal minor axis (termed thickness h here), such that $\frac{2R}{d_0} \simeq We^{1/2}$, indicating the prevalence of non-linearity. A similar observation has also been reported in numerical calculations [1]. There exists a critical We=1.36 (in our experiments) beyond which the droplet can no longer attain steady deformation (termed stable droplet), but instead continues to elongate (termed unstable droplet), ultimately leading to its breakup.

B. Droplet flattening

Figure S3 shows the side view visualisation of the different types of breakup of an acoustically levitated droplet depending upon the We. A better understanding of the droplet stretching in the stretching regime is seen in figure S3 (b) and (c) which shows the evolution of diameter (2R) as a function of time for different We for the stretching (flattening) and thinning regimes just before the initiation of atomization. A dotted line separates the stretching and thinning regimes. The stretching time reduces with an increase in the We (initial diameter of the droplet). There is a good agreement between the experiment and the deformation predicted by equation 5.11 in the main manuscript.

Note that the droplet is placed at the node of a standing sound wave, where the pressure is zero and the associated velocity field in the air is maximum. This velocity field of air, associated with the sound wave, alternates sinusoidal in time and acts as the ambient air velocity field in which the droplet is placed. When the droplet is placed at the node, it can be likened to a problem of a droplet placed in an oscillatory uniform velocity field, wherein the droplet disturbs the ambient velocity field. The resulting oscillatory velocity field is such that when air goes around the droplet, it creates stagnation points at the poles, generating positive pressure fields. Importantly, the air velocity is maximum at the equator, although oscillatory, which creates a non-oscillatory low-pressure region at the equator, consistent with the Bernoulli equation. It is this low pressure, created at the equator of the droplet, that leads to the flattening of the droplet.

C. Droplet Thinning

Figure S4 shows the dynamics of the radial expansion of the liquid sheet in the thinning regime. Both the top and side view digital images at time intervals of 7.14 μs are shown in Figure S4. The image has been recorded with the camera focused at the equatorial region to capture the non-linear interfacial instability developed on the thinned liquid sheet. The imaging provides insight into the mechanism underlying the equatorial atomization.

D. Breakup due to Faraday instability at the thinned equatorial region before rim breakup

Figure S5 shows the merging of the interconnected ligaments generated during liquid sheet perforation at the equatorial region. The ejection of the tiny-sized droplet due to Faraday instability causes sheet perforation. The resulting interconnected ligaments merge and break into droplets due to the RP instability.

E. Secondary breakup of different kinds

Figure S6 shows the formation of a convexly deflected stretched droplet sheet, undergoing secondary breakup after the equatorial breakup. The bag formation starts when the radial rim velocity decreases during the deceleration of the liquid sheet. At this stage, the liquid atomisation stops which indicates the domination of the capillary force over the inertial force i.e decrease of W_{eL}. The acoustic levitator can levitate the droplet only half of its wavelength i.e $\lambda/2 = 4.4$ mm. The sheet diameter is larger than half

of the wavelength and therefore, the pressure difference between the center and edge of the liquid sheet causes the sheet to bend upwards, resulting in the formation of a convexly shaped, deflected, stretched droplet sheet. This can be seen in figure S6 in the last image, where the arrow indicates a downward direction).

E.1. Umbrella breakup

Figure S7 shows the instantaneous digital images of the umbrella breakup of the liquid sheet after the equatorial breakup. The reader is suggested to see the corresponding movie 3 for more clarity. The images are recorded at 48k frames per second and presented at a time interval of 0.4 ms.

E.2. Bag breakup

Figure S8 shows the top view visualisation of bag breakup regimes after complete equatorial breakup. At this stage, the stretched liquid sheet starts to bend upwards to a convex shape.

E.3. Bubble breakup

Figure S9 shows the top view visualisation of bubble breakup after equatorial atomisation. The bubble expands in the radial direction, further reducing the thickness of the liquid sheet. Therefore, the liquid sheet achieves sub-harmonic conditions and Faraday waves are developed on the surface of the bubble.

E.4. Multi stage breakup

Figure S10 shows the top view visualisation of multistage breakup of acoustically levitated droplets.

4. DISCUSSION

A. Fragmentation at the rim of the equatorial region: Rayleigh Taylor instability

Figure S11 illustrates the top-view visualization of ligament formation in the radial direction and its subsequent breakup into droplets due to RT instabilities. The images are presented at a fixed time interval of $\Delta t = 69$ μs. The RT breakup takes over after the rim detachment. The RT instability is also responsible for the rim deformation.

B. Mechanism of secondary breakup

B.1. Mechanism of bag breakup

Figure S12 shows the droplet ejection perpendicular to the liquid sheet during bag development. This droplet ejection is captured during bag formation at very high frame speeds and can be seen in movie 5.

Figure S13 shows the formation of holes due to Faraday ejection of droplets and the subsequent growth of the holes with time.

B.2. Mechanism of bubble breakup and multistage breakup

Figure S14 shows images of the growth of Faraday instability on the bubble surface and indicates how the instability eventually results in the creation of a hole. Figure S14 also shows various nonlinear Faraday wave patterns on the bubble surface.

5. DROPLET SIZE DISTRIBUTION

We measured the size of the droplet generated during atomisation in different modes of the breakup. Figure S15 shows the generation of the larger-sized droplet due to the collision of droplets during equatorial atomisation. This is because the traveling velocities of the droplets are different in radial direction. Figure S16 shows the capillary regime of the equatorial breakup. Here, the breakup is completely dominated by RP instability.

6. STABILITY OF THE THIN LIQUID SHEET

We have used stability chart given by [2] to verify the unstable mode of the liquid sheet during wave formation on the liquid sheet. For this, the parameters p and q, are defined as,

$$p = 4k\frac{tanh(kh)}{\omega^2}\left(g + \frac{k^2\sigma}{\rho_L}\right) \tag{S1}$$

$$q = 2ka_p\frac{tanh(kh)}{\omega^2} \tag{S2}$$

have to be determined. The particle displacement in the acoustic field is given by,

$$\delta = \frac{P_0}{\rho_a c_0 \omega} = 23\mu m \tag{S3}$$

The acceleration of the particle can be calculated as,

$$a_p = \frac{\nabla_P}{\rho_a} = (i\omega)^2\delta = \omega^2\delta = 1451333.12 m/s^2 \tag{S4}$$

Where, P_0= 2400 Pa, $k = \frac{2\pi}{\lambda}$ and $\lambda = 65\mu m$, h = 8.5 μm, $\omega = 2\pi f$, f = 40000 Hz, c_0 = 340 m/s, σ = 22 mN/m, ρ_a = 1.22 kg/ m^3, ρ_L = 830 kg/ m^3 This yields, p = 1.024 and q = 3.

Figure S17 shows the location of p and q, on the stability diagram of [2] , indicating that the system, for the said conditions, falls within the unstable region (sub-harmonic). This provides further evidence that the Faraday instability is responsible for the capillary wave development on the liquid surface and the ejection of tiny droplets perpendicular to the liquid sheet.

REFERENCES

1. C. Lee, A. Anilkumar, and T. Wang, "Static shape and instability of an acoustically levitated liquid drop," Phys. Fluids A: Fluid Dyn. **3**, 2497–2515 (1991).
2. T. B. Benjamin and F. J. Ursell, "The stability of the plane free surface of a liquid in vertical periodic motion," Proc. Royal Soc. London. Ser. A. Math. Phys. Sci. **225**, 505–515 (1954).

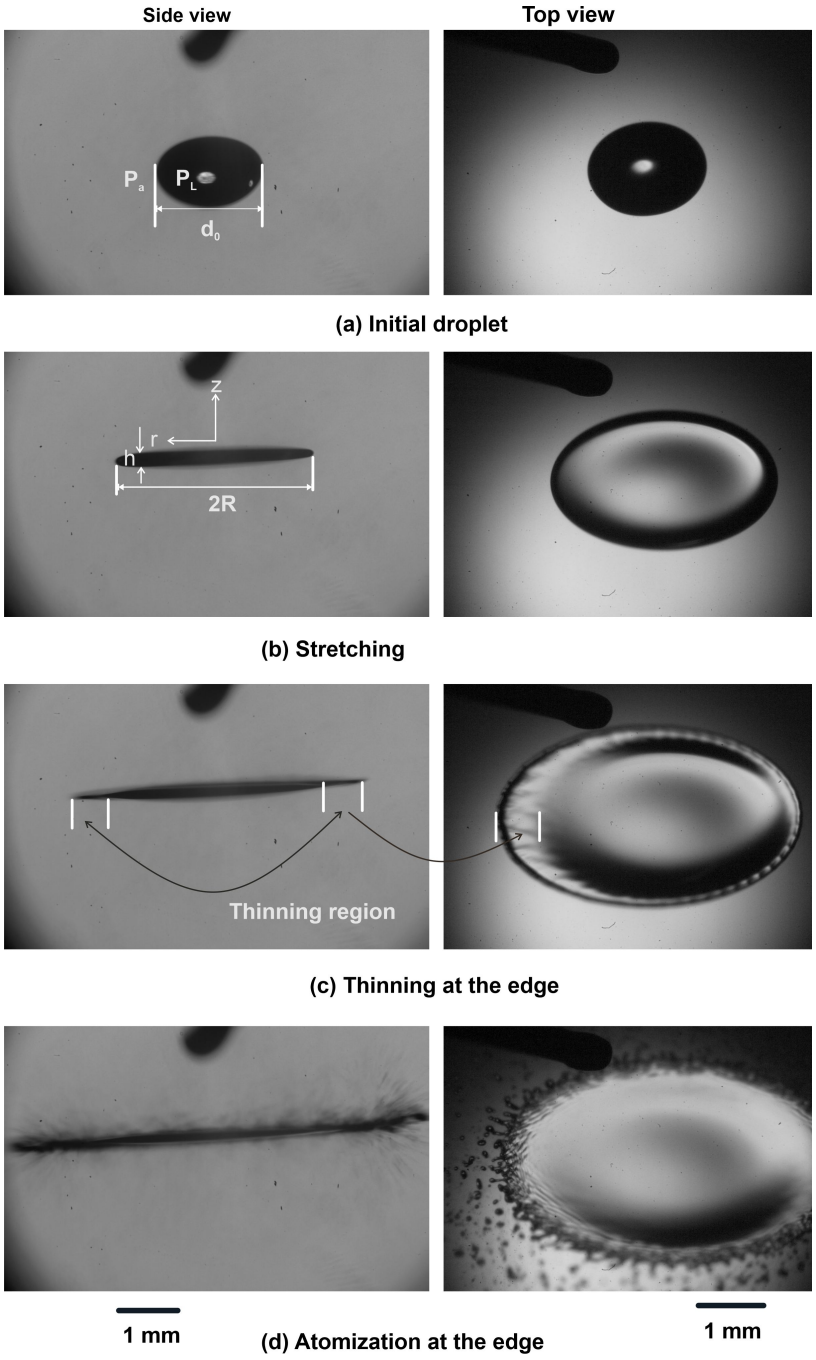

Fig. S1. Side view and top view images of an acoustically levitated droplet undergoing atomisation in different regimes: (a) initial droplet levitation in the acoustic field, (b) droplet flattened into a disc shape, (c) thinning at the edge, and (d) atomisation at the edge). The side view images are captured at 6,200 fps and the top view images are captured at 14,485 fps.

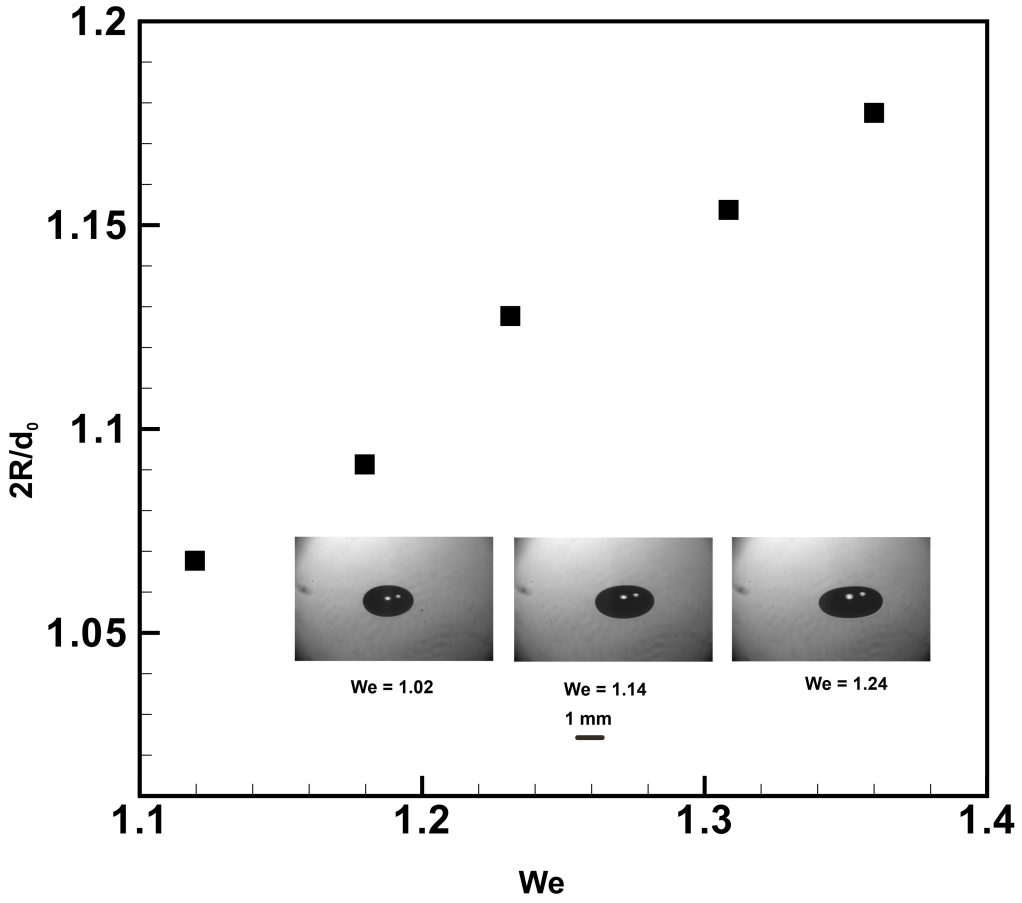

Fig. S2. Static deformation of an acoustically levitated droplet as a function of We. The captured images are provided inside the figure at different We.

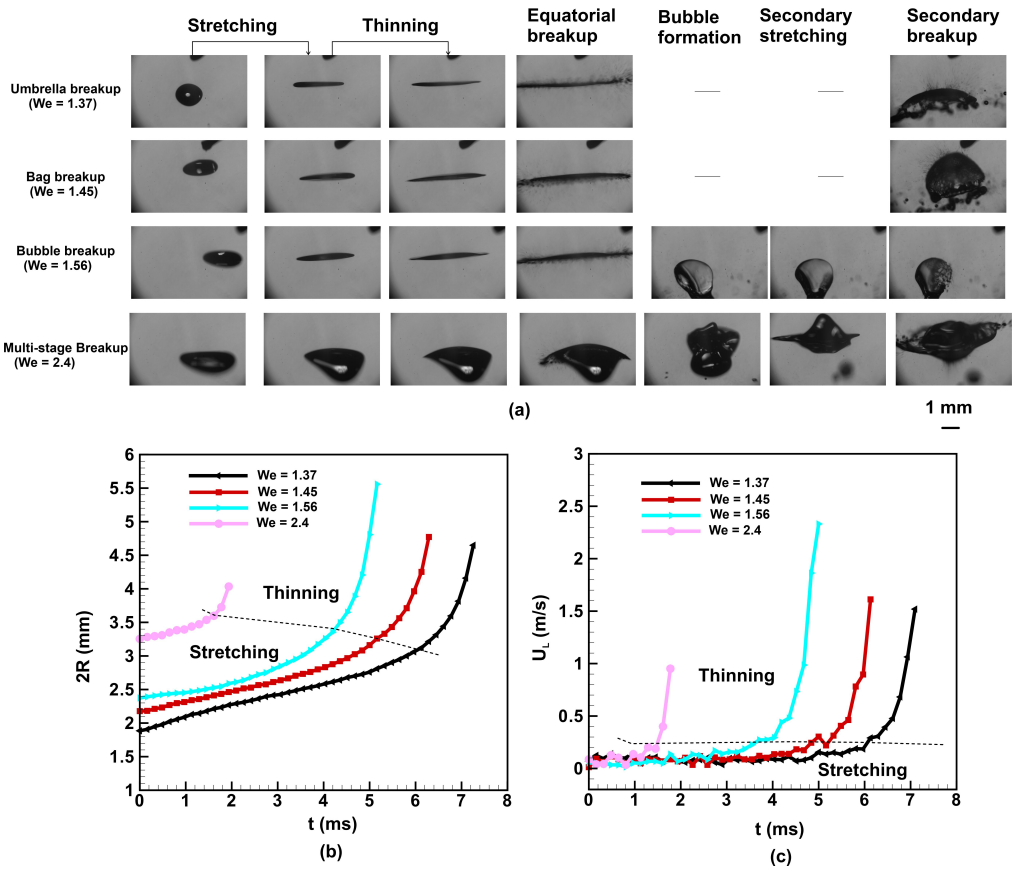

Fig. S3. (a) Side view visualization images at different *We* up to secondary breakup, (b) Evolution of the diameter of the droplet and (c) corresponding rim velocity at different times for various We. Note: the images have been recorded at 6200 fps and the respective video is movie 1.

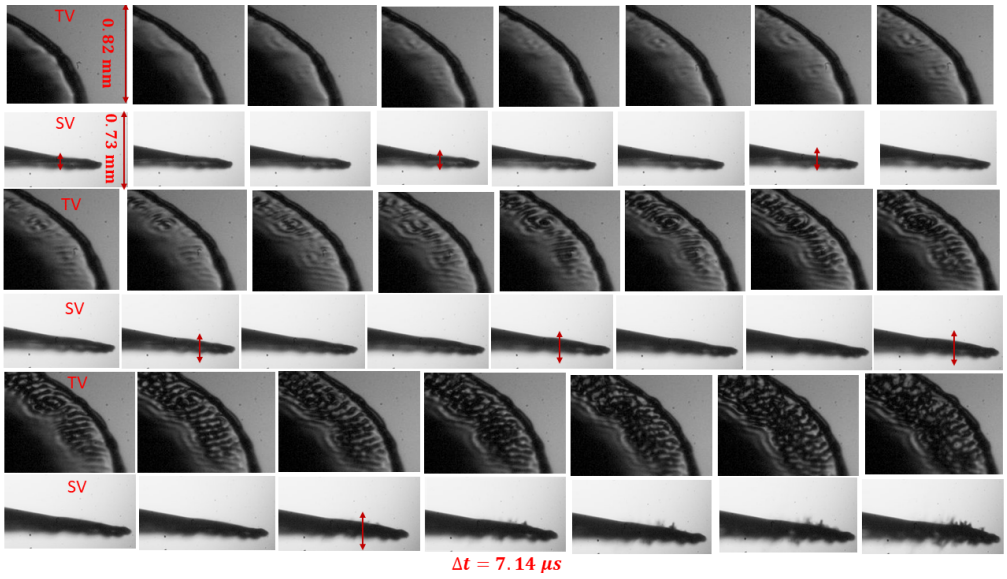

Fig. S4. Instantaneous top and side view digital images recorded at 140,000 frames per second in the thinning regime. The images are recorded focusing at the equatorial region. Here, TV and SV indicate the top and side views, respectively. The corresponding top and side view video can be found in movie 2. The vertical red arrows of side view images indicate the oscillations of liquid sheet in vertical direction .

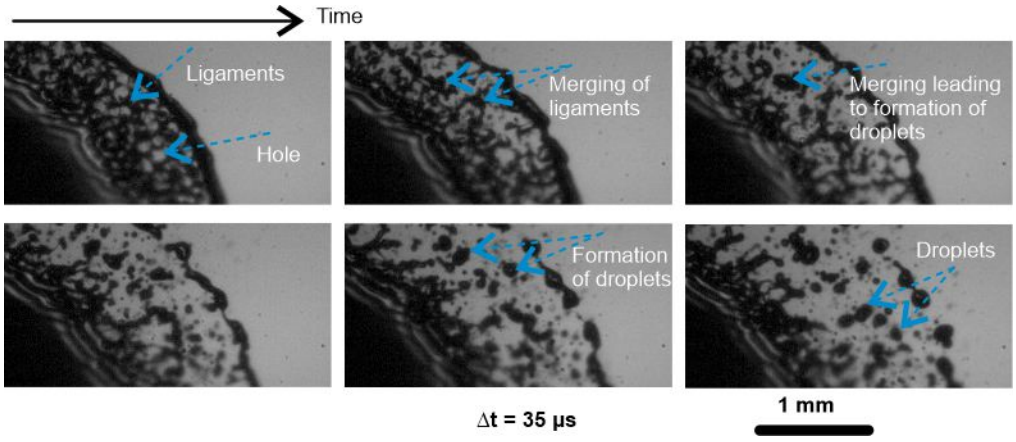

Fig. S5. The merging of interconnecting ligaments caused by the ejection of tiny-sized droplets perpendicular to the liquid sheet during equatorial atomization. The ligaments merge and break into the spherical droplets due to RP instability.

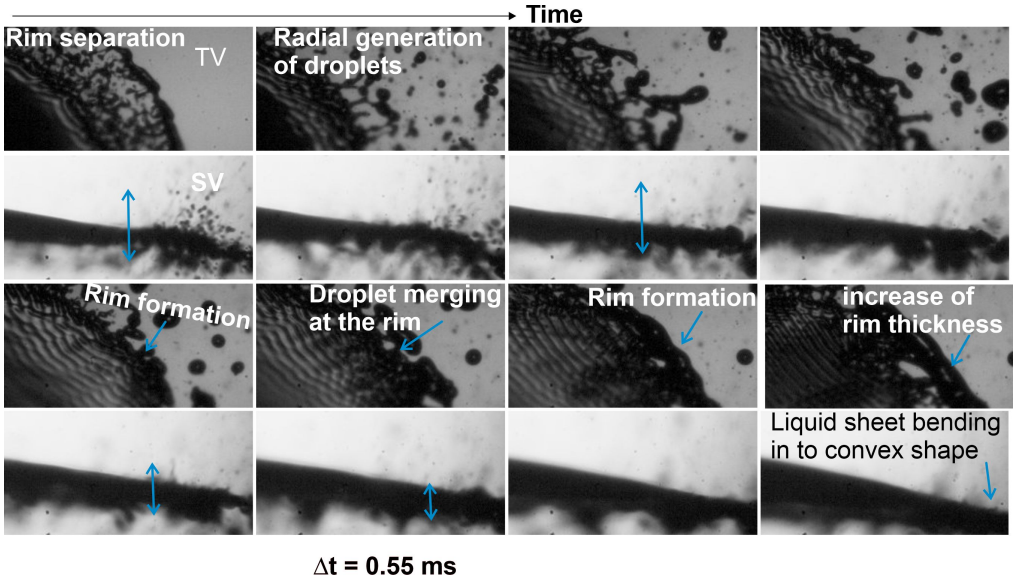

Fig. S6. Instantaneous top and side view digital images during equatorial fragmentation, which transforms the flattened droplet undergoing atomisation, into a flattened convexly deflected sheet when the atomisation stops. The vertical arrows indicate the vibration of the liquid sheet in the vertical direction. The readers are advised to see the movie 2 for more clarity.

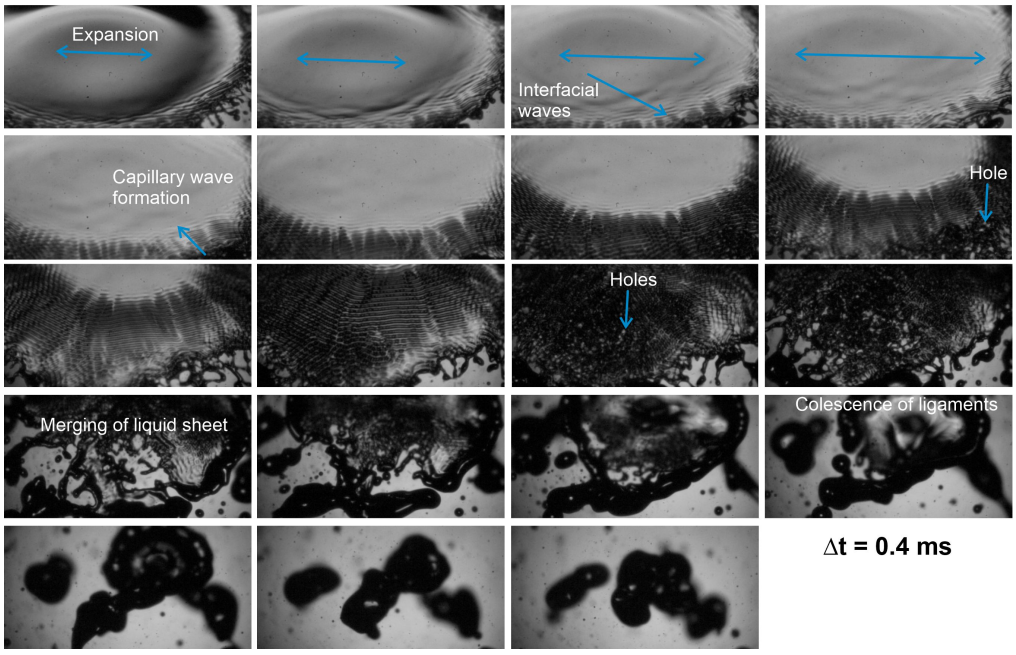

Fig. S7. Instantaneous top view digital images during umbrella breakup regime. The images are presented after the equatorial breakup at the $\Delta t = 0.4$ ms interval and explain the secondary atomisation. The corresponding video is available as umbrella breakup in movie 3.

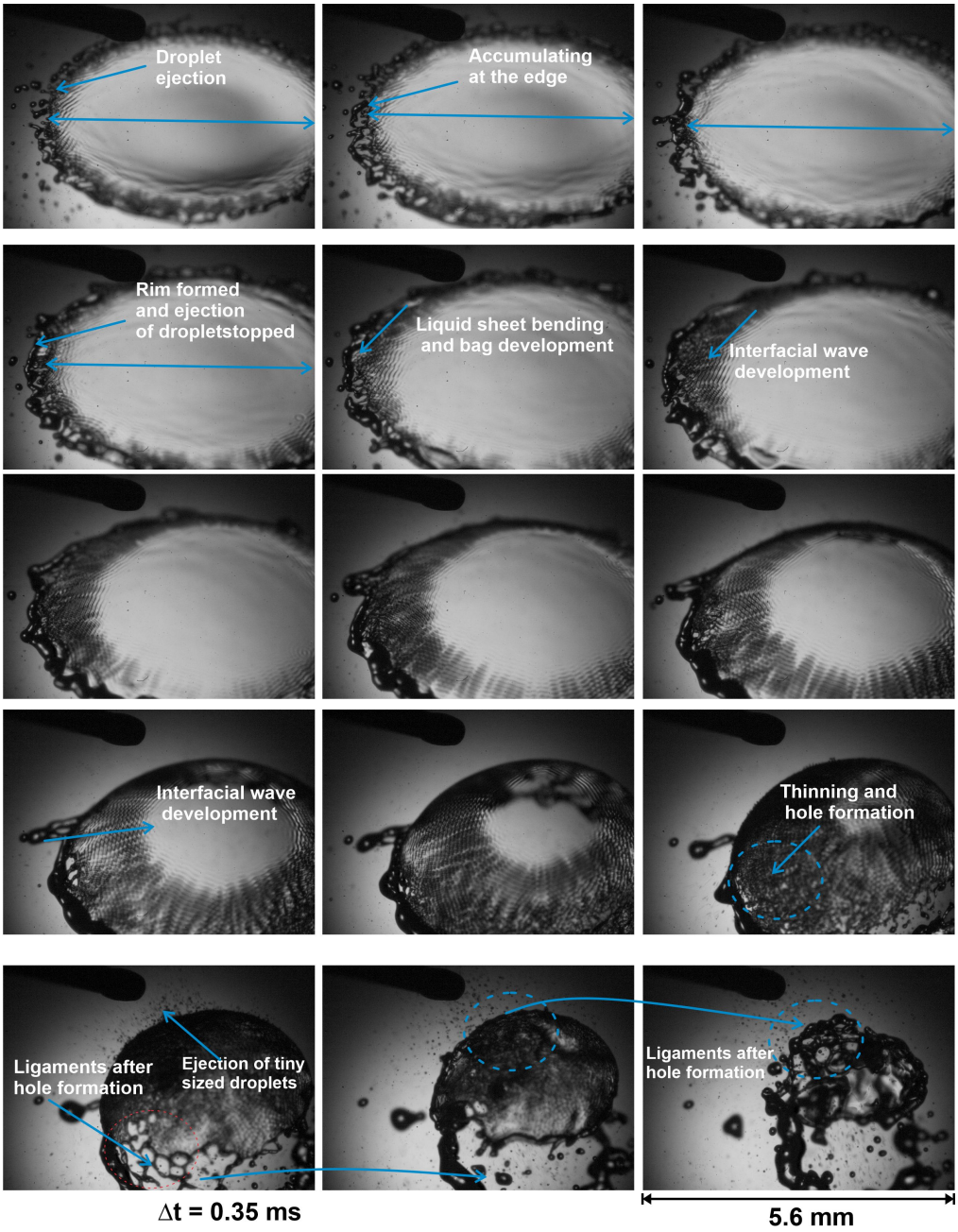

Fig. S8. Instantaneous top view digital images during bag breakup regime. The images are presented after the equatorial breakup at $\Delta t = 0.35$ ms. The corresponding video is available as bag breakup in movie 3. The top view of the digital images is recorded during bag formation at 14,485 frames per second and displayed at 0.35 ms intervals.

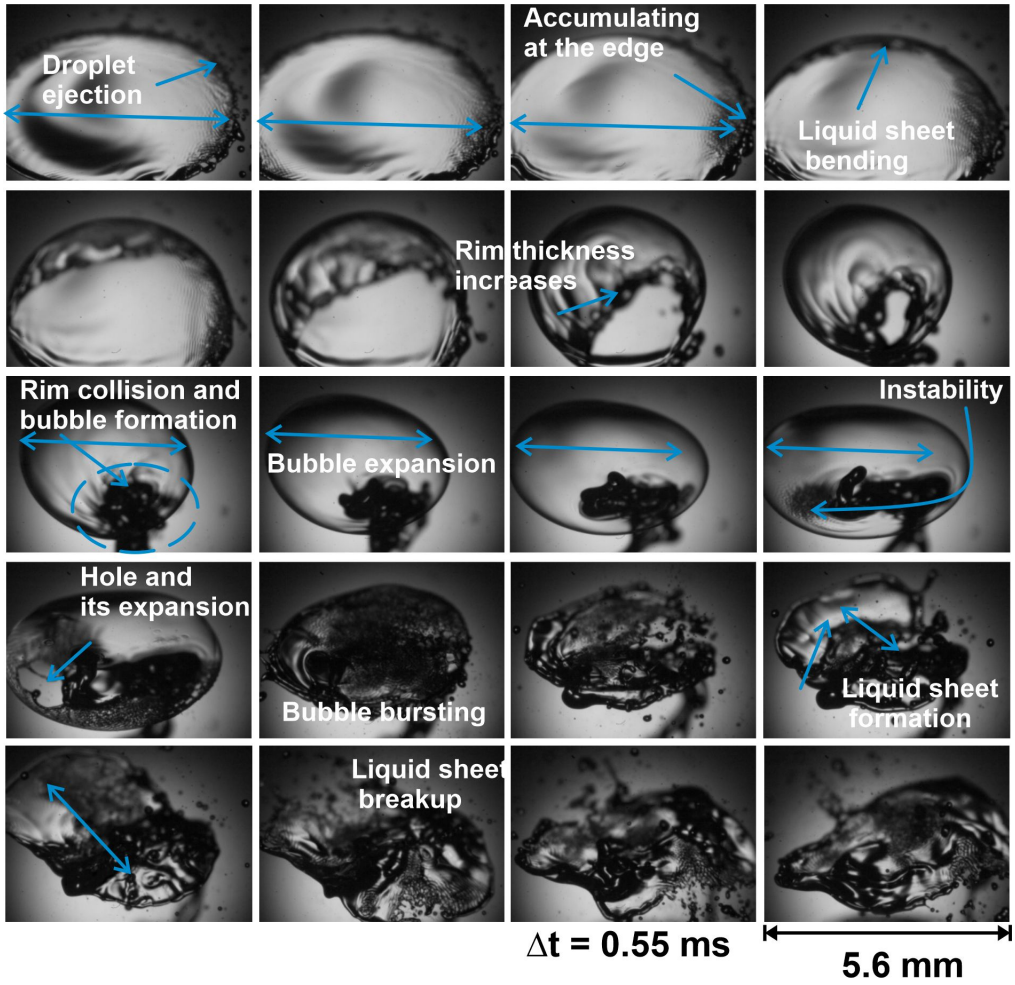

Fig. S9. Instantaneous top view digital images during bubble breakup regime. The images are presented after the equatorial breakup at $\Delta t = 0.55$ ms. The corresponding video is available as Bubble breakup in movie 3.

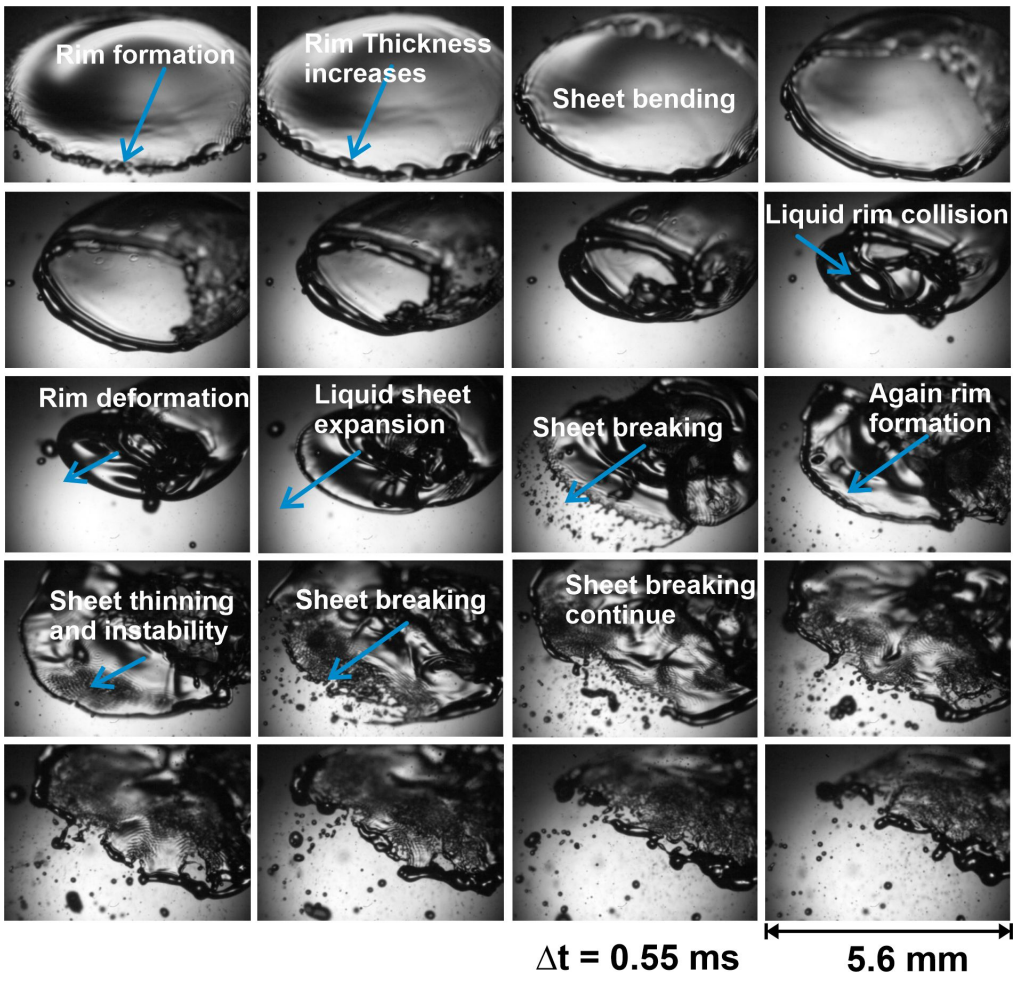

Fig. S10. Instantaneous top view digital images during multistage breakup regime after the equatorial atomization. The images are presented at a time interval of $\Delta t =$ 0.55 ms. The corresponding video is available as multi-stage breakup in movie 3.

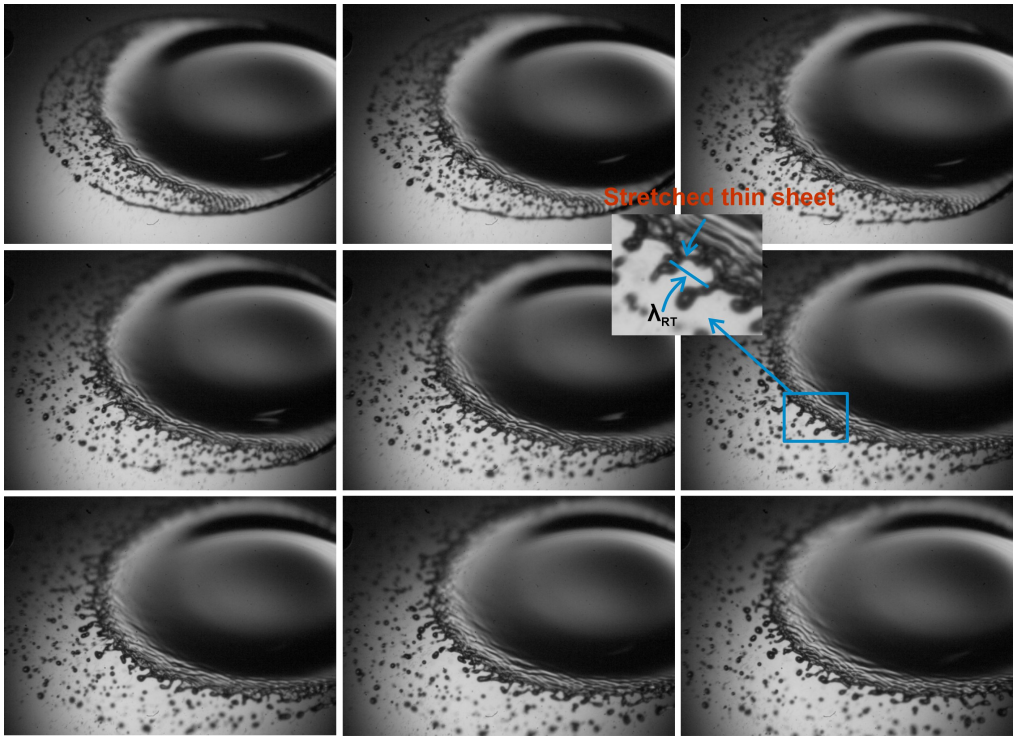

Fig. S11. Instantaneous top view digital images during breakup at the equatorial region. The images are shown at the time interval $\Delta t = 69\,\mu s$. The width of the image is equal to 5.62 mm. The corresponding video can be seen in movie 6.

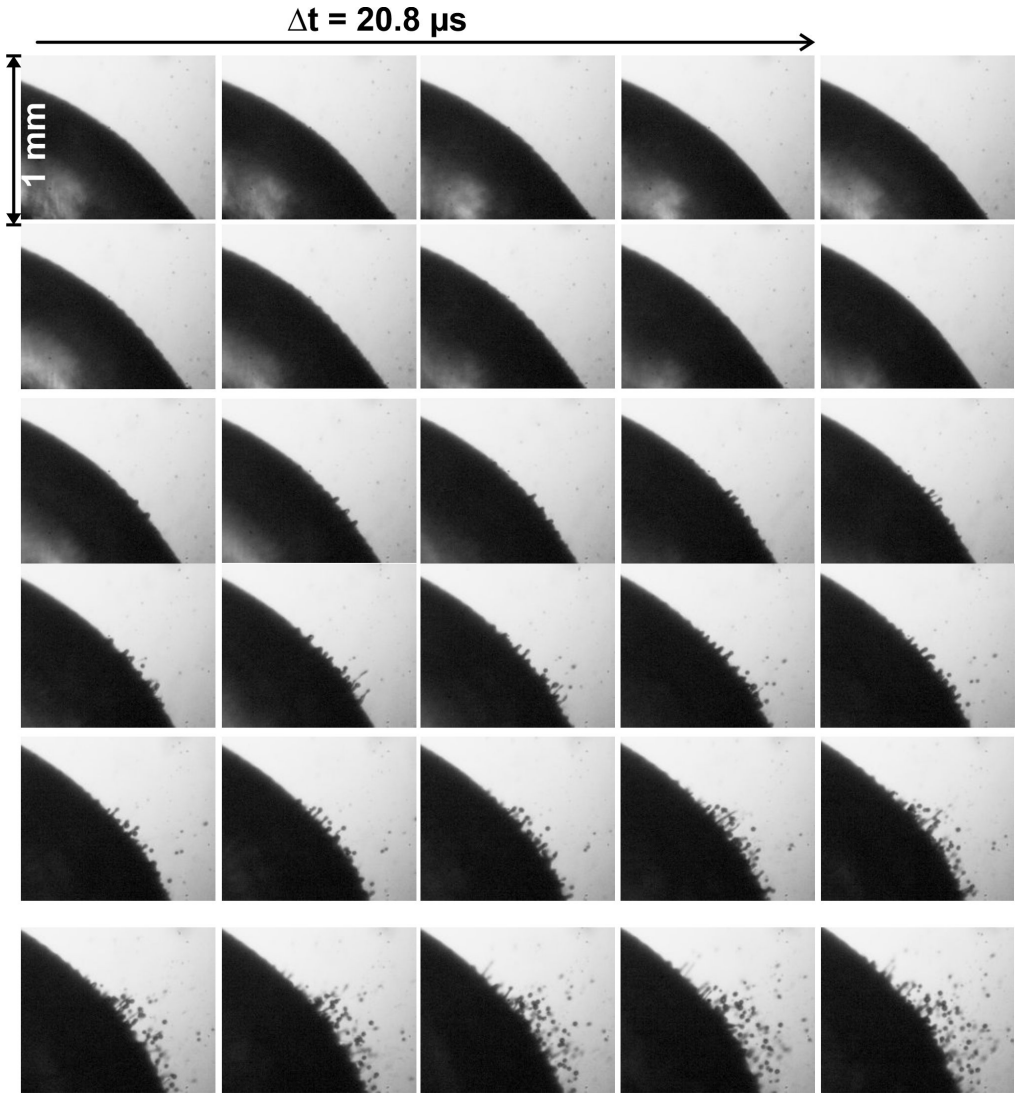

Fig. S12. Instantaneous side view digital images of droplet ejection during instability propagation in bag breakup regime. The images are presented at a time interval of 20.8 μs. The corresponding video is available in movie 5 during the bag breakup.

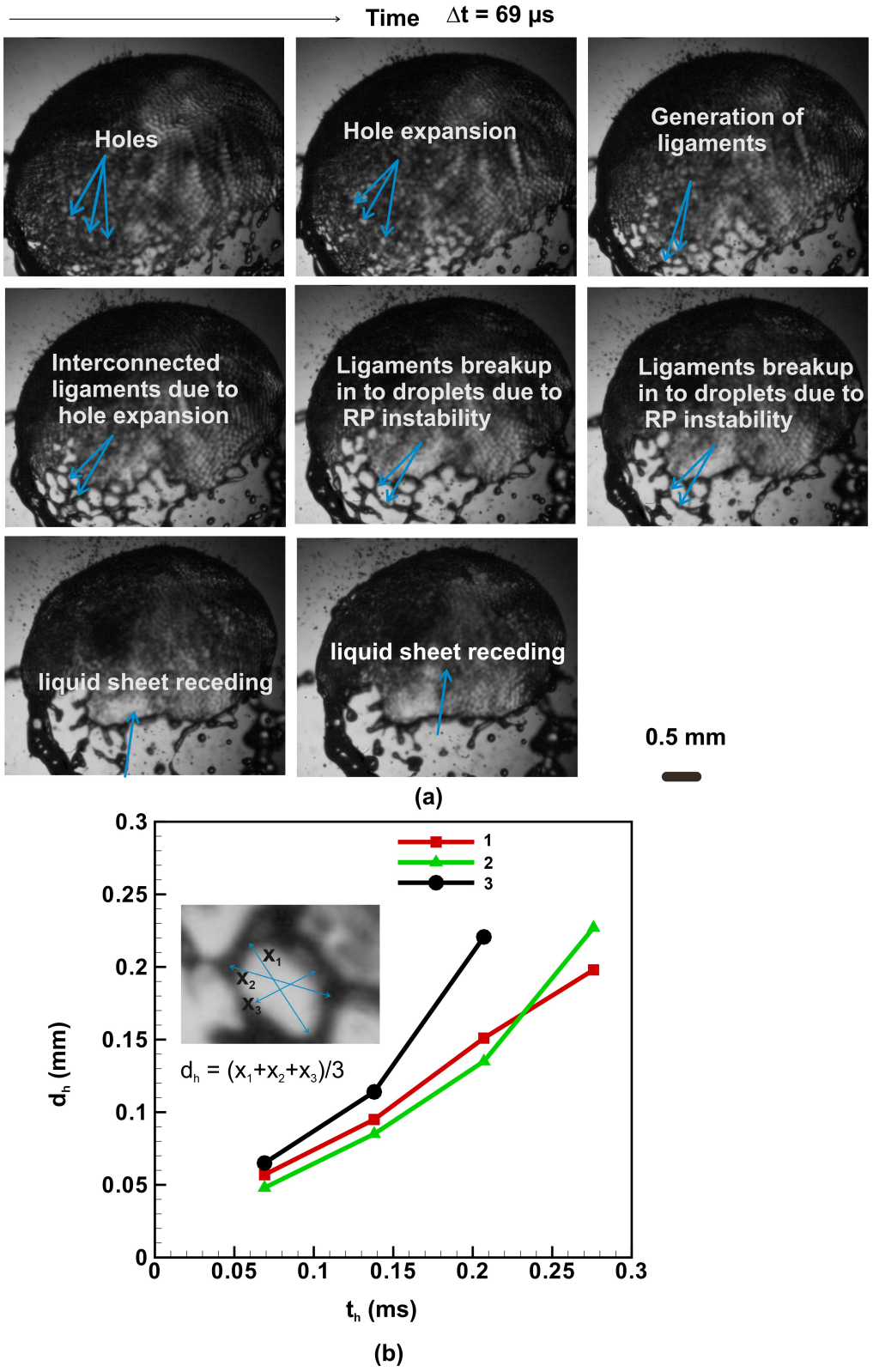

Fig. S13. Hole formation and ligament breakup during bag breakup regime: (a) visualization of top view images and (b) variation of hole expansion diameter with time. Here, d_h is the hole diameter and t_h is the time starting from the initiation of hole formation.

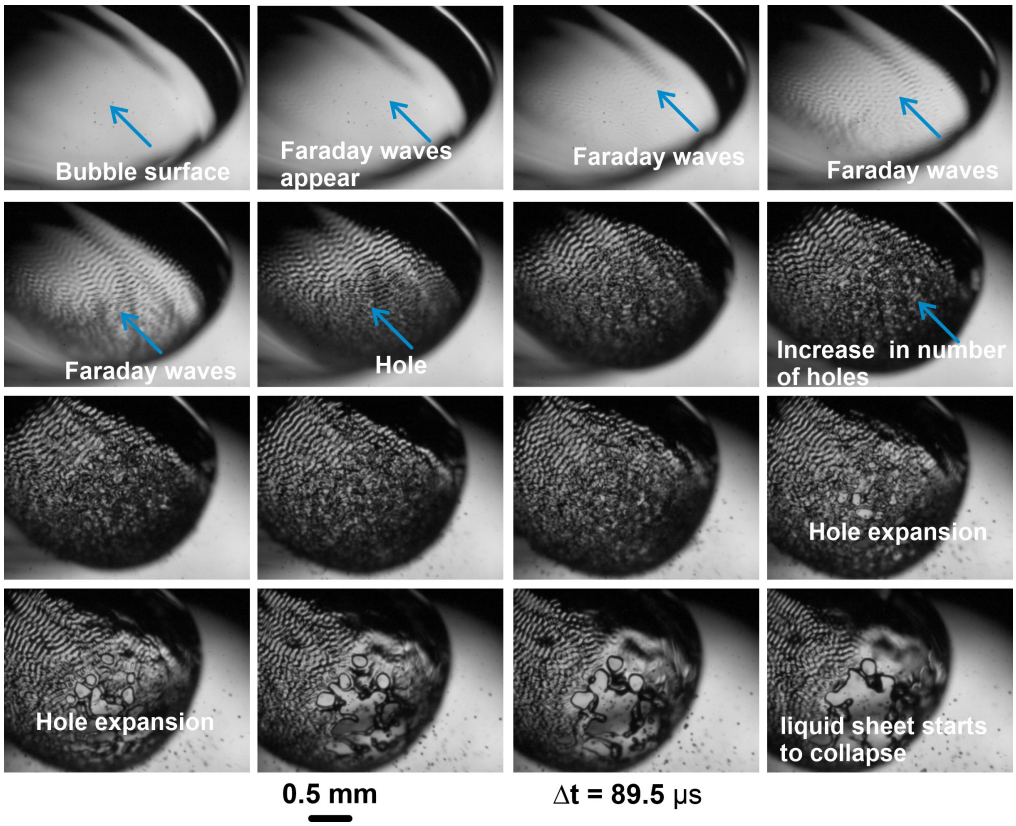

Fig. S14. Instantaneous images of the growth of Faraday instability on the bubble surface and how that instability eventually resulted in creating a hole. The corresponding video is available at movie 9.

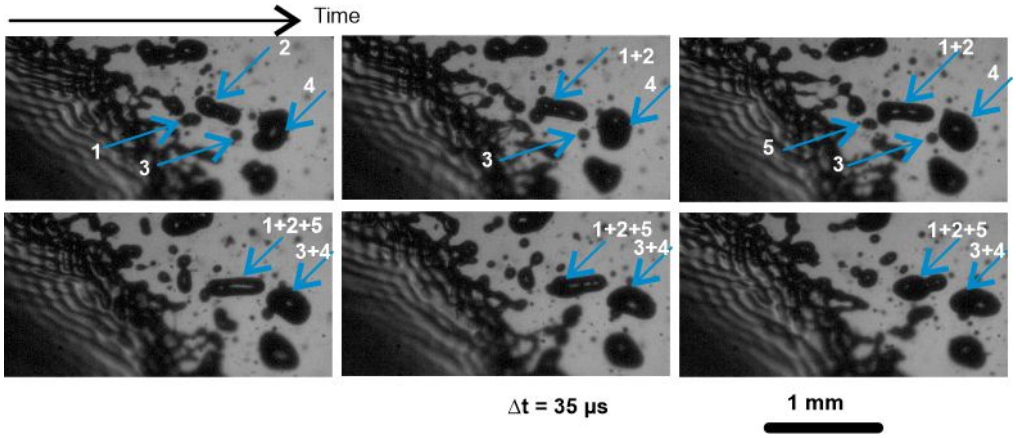

Fig. S15. Merging of two droplets in radial direction. The droplets are marked by a number for ease of tracking.

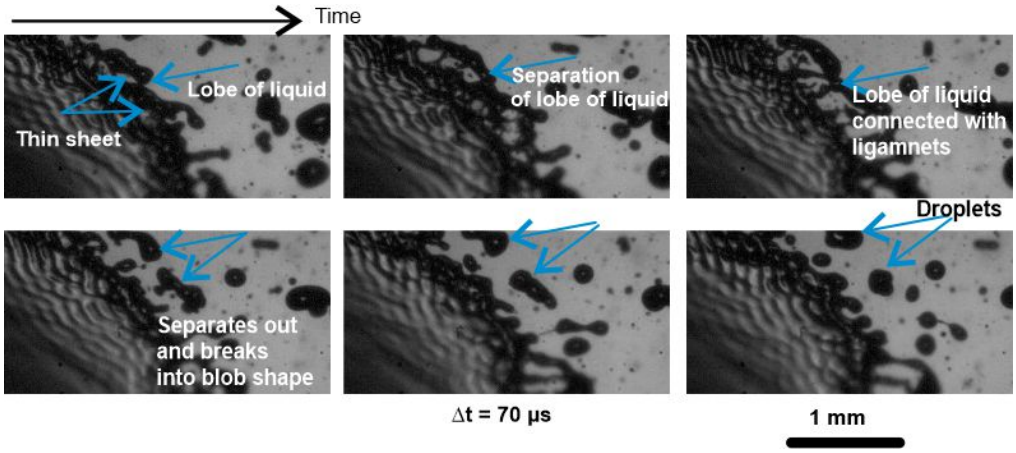

Fig. S16. Droplet generation at the late stage of the equatorial breakup (deceleration phase) when the expanding sheet has a much reduced radial velocity.

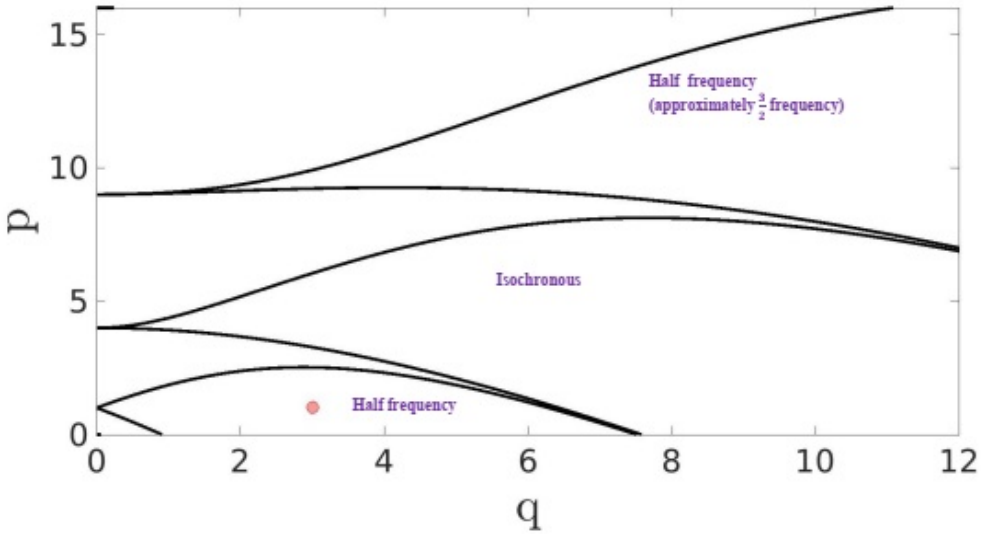

Fig. S17. The stability diagram for an acoustically vibrating sheet following the Mathieu's equation in the p and q coordinates, as described in [2]. The location of the experimental data point which corresponds to the condition of instability (sheet thickness h= 8.5 μm is shown in a dark red circle).